Precisely calibrated and spatially informed illumination for conventional fluorescence and improved PALM imaging applications

Angel Mancebo[1], Luke DeMars[1], Christopher T. Ertsgaard[1], Elias M. Puchner[1,#]

[1]School of Physics and Astronomy, University of Minnesota, Twin Cities, Physics and Nanotechnology (PAN), 115 Union Street SE, Minneapolis, MN 55455

Abstract

Spatial light modulation using cost efficient digital micromirror devices (DMD) is finding broad applications in fluorescence microscopy due to the reduction of phototoxicity and bleaching and the ability to manipulate proteins in optogenetic experiments. However, precise illumination by DMDs and their application to single-molecule localization microscopy (SMLM) remained a challenge because of non-linear distortions between the DMD and camera coordinate systems caused by optical components in the excitation and emission path. Here we develop a fast and easy to implement calibration procedure that determines these distortions and matches the DMD and camera coordinate system with a precision below the optical diffraction limit. As a result, a region from a fluorescence image can be selected with a higher precision for illumination compared to a rigid transformation allowed by manual alignment of the DMD. We first demonstrate the application of our precisely calibrated light modulation by performing a proof-of concept fluorescence recovery after photobleaching experiment with the endoplasmic reticulum-localized protein IRE1 fused to GFP in budding yeast (*S. cerevisiae*). Next, we develop a spatially informed photoactivation approach for SMLM in which only regions of the cell that contain photoactivatable fluorescent proteins are selected for photoactivation. The reduced exposure of the cells to 405 nm light increases the possible imaging time by 44% until phototoxic effects cause a dominant fluorescence background and a change in cell morphology. As a result, the mean number of reliable single-molecule localizations is also significantly increased by 28%. Since the localization precision and the ability for single-molecule tracking is not altered compared to traditional photoactivation of the entire field of view, spatially informed photoactivation significantly improves the quality of SMLM images and single-molecule tracking data. Our precise calibration method therefore lays the foundation for improved SMLM with active feedback photoactivation far beyond the applications in this work.

Introduction

Fluorescence microscopy techniques are continually advancing our understanding of cellular processes through the specific labeling and visualization of biomolecules within living cells. The quantitative analysis of this data provides valuable information about the complex spatial organization, dynamics and interactions of biomolecules, which are essential for all fundamental biological processes. In traditional confocal and epi- fluorescence microscopy applications, the excitation power is kept constant across the field of view. The resulting fluorescence intensity therefore correlates with the density of labeled molecules within a diffraction limited volume. Over the decades, however, many advanced imaging modes have been developed that rely on either excitation light being focused to a region of interest (ROI) within the sample or spatially-patterned illumination across the sample. Fluorescence recovery after photobleaching (FRAP) applications, for instance, utilize a small selected volume within the sample that is excited to locally deplete its fluorophores through bleaching. The diffusion coefficient and the immobile fraction of labeled biomolecules can then be determined based from the time and the fraction of fluorescence recovery within the ROI [1].

Patterning the excitation light within the sample plane has also found applications in active illumination fluorescence microscopy for long-term measurements. By actively regulating the excitation to keep a constant detection power across the field of view, detector saturation is avoided while maintaining sensitivity for weak signals [2,3]. The active patterning of light in the sample plane is not only used for imaging but also for manipulating proteins in optogenetic applications. By locally activating light sensitive ion channels or the interaction of regulatory proteins within a cell, important information about spatial aspects of cell signaling has been obtained [4–6].

While fluorescence microscopy techniques employing spatially patterned light excitation have made significant and valuable contributions to our understanding of cellular processes, they are all hampered by the diffraction-limited readout of the fluorescence signals. This limited resolution prevents resolving the myriad of intracellular structures and protein assemblies that are much smaller than the optical diffraction limit of ~250 nm. The advent of fluorescence super-resolution microscopy techniques overcame these limitations and allow us to resolve intracellular structures with ~20 nm resolution [7–10] and to quantify the biomolecules they contain [11–13]. SMLM methods, termed stochastic optical reconstruction microscopy (STORM) [7] and photoactivated localization microscopy (PALM) [8] are based on activating only a sparse subset of photoactivatable fluorophores in each frame either by photoswitching or by exploiting intrinsic dark states of the fluorophores [7,8,14]. Similarly, fluorogen activating proteins have been used to create spatially separated fluorescent bursts of transiently binding fluorogens [15,16]. The center location of individual fluorophores can then be determined with high precision by fitting each point-spread function in each frame. A super-resolution image is then built by combining the single-molecule localizations from numerous data acquisition frames.

In this work we present a simple computer-based calibration approach for a versatile, high-precision and low-cost setup that combines for the first time the advantages of spatially

informed illumination with SMLM imaging and patterning of the photoactivation laser. We first describe the construction of an excitation path comprising a Digital Micromirror Device (DMD) that can be added to existing fluorescence microscope setups. While DMDs have been used in the past in custom-made and commercial setups for patterned illumination [19–22] a persistent problem for SMLM and other high-precision applications is the nonlinear distortion between the DMD and the camera coordinate system caused by optical components. Our custom computer-based calibration determines and corrects for these distortions. As a result, the DMD pixels are matched to the camera pixels with a median and maximum deviation of 50 nm and 140 nm, respectively, which is well below the optical diffraction limit. This precision is more than 4-fold higher than a rigid transformation achievable with a perfect manual alignment of the DMD, which resulted in a median and maximum deviation of 230 nm and 530 nm, respectively. We demonstrate the applicability of the system for patterned illumination in live budding yeast cells (*S. cerevisiae*), a well-established eukaryotic model organism, which has been used extensively in super-resolution microscopy [11,23–26]. We demonstrate the versatility of this approach for patterned illumination applications by performing a proof of concept FRAP experiment. We further combine, for the first time, spatially informed illumination with SMLM by photoactivating only those regions within the cell where photoactivatable fluorescent proteins (PAFPs) are located. Patterning the excitation light has found some use in fixed-cell STORM applications to obtain a constant excitation power across large fields of view and to selectively excite regions of the sample [17,18]. However, the benefits of using DMDs with such high level of control and precision for patterning the phototoxic photoactivation light in live-cell SMLM applications have to our knowledge never been demonstrated. The high precision of our system enables confining the photoactivation as much as possible to the subcellular regions where PAFPs are located and thus reduces the overall exposure of cells to the high-energy photoactivation wavelengths. We demonstrate that patterned photoactivation significantly reduces background fluorescence caused by phototoxicity, increases the possible imaging time by nearly 44% and provides a 28% improvement in the number of detected single-molecule localizations compared to traditional photoactivation of the entire field of view. This increase in localizations improves the quality of super-resolution images as well as the accuracy of single-molecule tracking data. Our calibration method therefore presents a versatile, precise and cheap option for microscopy applications with actively patterned illumination and lays the foundation for improved SMLM with spatially informed illumination far beyond the demonstrated applications in this work.

Materials and methods

Experimental Setup

All conventional and super-resolution images were recorded on an inverted microscope (Ti-E; Nikon, Minato, Tokyo, Japan) with a Perfect Focus System to compensate for sample drift in the z-direction. All movies were recorded on an electron-multiplying charge-coupled device (EMCCD) camera (iXon 897 Ultra DU-897U; Andor, Belfast, United Kingdom). The camera was cooled down to –70°C. The EMCCD gain was set to 30 for all experiments except the bleaching portion of FRAP experiments for which it was set to 0 (no EMCCD gain).

Lasers (405 nm, 488 nm, 561 nm, OBIS-CW; Coherent, Santa Clara, CA) were combined with dichroic mirrors, aligned, expanded, and focused to the back focal plane of the objective (Nikon-CFI Apo 100x Oil immersion NA 1.49). The lasers' intensities were controlled by a computer via USB and were digitally-modulated using a NI-DAQ board (PCI-6221; National Instruments, Austin, TX) connected to the computer with programmed shutter sequences. The NI-DAQ board synchronized the lasers to the camera frame duration.

All illumination patterning was done with a DMD (DLP® LightCrafter 4500™; Texas Instruments, Dallas, TX) consisting of $912 \times 1,140$ square pixels arranged in a diamond configuration, with a refresh rate of 60 Hz. Each pixel has a side length of 7.639 μm, which corresponds to 114 nm in the sample plane. To specify the illumination, a binary mask is sent to the DMD using custom software written in Python. While in principle a binary mask can be created by thresholding a fluorescence image, we hand-drew the regions based on the fluorescence image for more control. The transformation is then applied to the pattern before sending it to the DMD to account for misalignments and distortions caused by the optical components between the DMD and camera. For PALM experiments, the expanded 405 nm laser was directed onto the DMD by mirrors with an angle of incidence of 24° to the DMD surface normal. This angle is the blaze angle of the DMD and is required to maximize diffraction efficiency and for the reflection to be parallel to the DMD surface normal. The diffracted light from the DMD was captured by a 4F system consisting of a lens of 1 in diameter and focal length of 50.2 mm, a mirror mounted at an angle of 45° and a lens of 2 in diameter and focal length of 150 mm. This 4F system serves two purposes: to capture the diverging orders of the DMD near the source, maximizing power transmission, and to form the DMD image in the focal plane of the microscope lens. A longpass dichroic filter (ZT405rdc; Chroma, Bellows Falls, VT) was used to combine the patterned light of the 405 nm laser with the 488 nm and 561 nm beams before they are focused by a lens of 2 in diameter and focal length of 400 mm to the back focal plane of the microscope objective (see Fig. S1). For FRAP experiments, a longpass dichroic filter (ZT488rdc; Chroma, Bellows Falls, VT) was used instead to direct the patterned light of the 488 nm laser into the microscope.

For two-color imaging of red (595 nm) and green (525 nm) fluorescence, the fluorescence emission was split by a dichroic longpass beamsplitter (T562lpxr BS; Chroma, Bellows Falls, VT). The emission in each channel was further filtered by bandpass filters: ET525/50m (Chroma, Bellows Falls, VT) in the green channel and ET595/50m (Chroma, Bellows Falls, VT) in the red channel.

To estimate the power density of the lasers at the sample plane, we measured the intensity after all neutral density filters but before the beam expander with a power sensor (S130C; Thorlabs, Newton, NJ) and divided by the illumination area in the sample plane. The typical power density for 561 nm excitation of single molecules was 428 W/cm^2 and for conventional 488 nm excitation 0.15–0.45 W/cm^2. To estimate the power density of patterned light, we measured the emission of a fluorescein dye solution with 405 nm excitation. The DMD power density was then calculated by multiplying the power density without the DMD by the mean ratio of the emission intensities with and without the DMD. The typical power density of patterned 405 nm activation (which was gradually increased

during each PALM experiment to maintain the activation rate) was 3.6 mW/cm^2-177 W/cm^2. The power density of patterned 488 nm excitation for bleaching in FRAP was 89 W/cm^2. The power density for initial fluorescence and fluorescence recovery measurements in FRAP was 1.7 W/cm^2.

Sample preparation

Concanavalin A (ConA)

Cells were immobilized to the chambered coverglass surface by using a solution of ConA in deionized water (0.8 mg/mL; Sigma-Aldrich, St. Louis, MO) which was incubated on the coverglass surface. After at least 30 minutes, excess ConA was withdrawn and the slide was rinsed three times with deionized water prior to plating the cells. Diluted cells were allowed to settle and bind to the ConA on the surface for at least 20 minutes before imaging.

DMD Calibration

Calibration was performed by projecting the calibration pattern with 405 nm excitation onto a coverslip with a solution of fluorescein dye (10–20 μL of 130 μM; Sigma-Aldrich, St. Louis, MO).

FRAP

FRAP experiments were performed using a W303 MATa (MATa ura3 trp1 leu2 his3 ade2 can1, Horizon-Dharmacon, YSC1058) *S. cerevisiae* strain. The ade2 mutation in the purchased strain was repaired by PCR-mediated transformation. Wild-type ADE2 was amplified from genomic DNA, RB201 (W303 MATa, trp1, leu2, ura3, his3, can1R, ADE2) with Phusion PCR (NEB) using the forward primer (ATGGATTCTAGAACAGTTGGTATATTGGGAGGGGGACAA) and the reverse primer (TTACTTGTTTTCTAGATAAGCTTCGTAACCGACAGTTTCTAACTT). To label IRE1 with GFP (IRE1-GFP-IRE1), the native IRE1 gene was knocked out by a PCR-mediated gene deletion using the pFA6a-kanMX6 template [27] and forward primer: CCTTCATACACATTAAAAAAACAGCATATCTGAGGAATTAATATTTTAGCACTTTGA AAAtacgctgcaggtcgacgg and reverse primer: ATGATCAAAGTAACATTAATGCAATAATCAACCAAGAAGAAGCAGAGGGGCATGA ACATGcatcgatgaattcgagctcg. The knockout was confirmed by colony PCR. Next, the IRE1 promoter (1346 base pairs upstream the start codon) and the IRE1 gene until the Juxtamembrane position, which is a tagging site that does not interfere with the function of IRE1 [28], was PCR amplified from W303 genome using forward primer: TCGTA GGGCCC GTCGTGCTATGTTGAGAAACGA to introduce the ApaI restriction site and the reverse primer: ACATTCTCGAGACCAGATCCAATTTTGGATAATAATACATA at the Juxtamembrane position to introduce the XhoI restriction site. yeGFP was PCR amplified using the forward primer: TCGTA CTCGAGatgtctaaaggtgaagaattattca to introduce the XhoI restriction site and the reverse primer: AATGTGGATCCtttgtacaattcatccatacc to introduce the BamHI restriction site. The remaining IRE1 gene up to the stop codon was PCR amplified with the forward primer TCGTAGGATCCGGATTTATGCCTGAAAAGGAAAT to introduce and additional BamHI restriction site and reverse primer TCGTAGCGGCCGCTTATGAATACAAAAATTCACGTAAA to introduce a NotI

restriction site after the stop codon. PCR products were assembled in pNH605 yeast integration plasmid that targets the LEU2 locus [29] and transformed in the W303 IRE1 knockout strain. Integration was confirmed by colony PCR and fluorescence imaging.

The cells were inoculated in synthetic complete dextrose (SCD) medium to an optical density of 0.28 and grown overnight in a shaking incubator at 270 rpm and 30 °C. The cells were diluted to an optical density (OD) of 0.29 in the morning and grown in the shaking incubator under the same conditions for 3.5 hours until and OD of 0.78 was reached. The cells were again diluted to an OD of 0.31 and after 2.5 hours, the cells reached an OD of 0.72. The cells were then diluted 1:7 to achieve an OD of 0.1 and 210 μL were plated and allowed to settle for at least 20 minutes.

PALM

PALM experiments were performed using a W303 *S. cerevisiae* strain (pSte5_mEos2–3x_PH2x) [30] with a triple-repeat of mEos2 fused to the plextrin homology (PH) domain of Plc(delta1), which localizes to the plasma membrane. The construction of this yeast strain was previously published in reference [30] and for this study we replaced the weak pINO promoter with 511 bases of the stronger pSte5 promoter (W303 genome). The cells were inoculated in SCD medium to an optical density of 0.13 and grown overnight in a shaking incubator at 270 rpm and 30 °C. The cells were diluted to an OD of 0.23 in the morning and grown in the shaking incubator under the same conditions for 4 hours to OD 0.72. To locate the plasma membrane for patterned photoactivation during PALM imaging, the yeast cell wall was stained with ConA-CF488M (Biotium, Fremont, CA) which is a 488 nm-excitable dye conjugated to ConA. The cells were incubated at an OD 0.1 for 30 minutes in SCD containing 33 μg/mL of ConA-CF488M in a shaking incubator at 270 rpm and 30 °C.

Data acquisition and analysis

DMD Calibration

To precisely map the DMD pixels to the camera pixels, a grid of spots was sent to the DMD and the reflected 405 nm laser was projected onto a sample of fluorescein dye solution. For this task, the pattern must extend throughout the entire field of view. For simplicity, a 4×4 grid of spots was used for calibrating the DMD before all live cell experiments. The resulting emission spots with 1.83 μm diameter and 9.53 μm center-to-center spacing were recorded at 5 Hz for 50 frames and the frames were averaged to reduce camera noise. Both the microscope image and the projected image were processed by the software, which detects the spots' coordinates (Fig. 1 A and S2). This custom software is written in Python and leverages the OpenCV [31] and scikit-image [32] libraries for computer vision and image processing. The software determines the centroid of each spot by blob detection in the microscope image. The detected spots are subsequently fit to Gaussians within a window of twice the estimated spot size. The software for warping and sending images to a DMD and for determining the transformation between a projected image and its corresponding microscope image will be freely available for download on GitHub.

The transformation between the centroids of the spots in the projected image and the microscope image are determined by first sorting the coordinates in two dimensions to ensure the correct correspondence between projected spots and detected spots. After sorting, one set of coordinates is fit to the other by a 3rd-order polynomial of the form shown in Eq. 1,

$$\begin{bmatrix} x' \\ y' \end{bmatrix} = \begin{bmatrix} \theta_{00} & \theta_{01} & \theta_{02} & \theta_{03} & \theta_{04} & \theta_{05} & \theta_{06} & \theta_{07} & \theta_{08} & \theta_{09} \\ \theta_{10} & \theta_{11} & \theta_{12} & \theta_{13} & \theta_{14} & \theta_{15} & \theta_{16} & \theta_{17} & \theta_{18} & \theta_{19} \end{bmatrix} \begin{bmatrix} 1 \\ x \\ y \\ x^2 \\ xy \\ y^2 \\ x^3 \\ x^2y \\ xy^2 \\ y^3 \end{bmatrix} \tag{1}$$

where (x, y) and (x', y') are the source and destination coordinates, respectively, and $\{\theta_{ij} \mid 0 \le i \le 9$ and $j = 0,1\}$ are the weights for each term in the polynomial transformation that are determined during fitting. Since we compensate for distortions by using the inverse transformation, the source and destination correspond to the camera and DMD, respectively. To verify the accuracy of the transformation and to estimate its precision, we warped the original calibration pattern by applying the inverse transformation to it and sent the warped calibration pattern to the DMD. The warped calibration pattern was projected onto the dye sample, the emission was recorded, and the original calibration pattern and microscope image were processed as previously described in the DMD calibration section (see Fig. S2). The median distance between corresponding points of the original calibration pattern and the camera image was well below the theoretical diffraction limit of ~200 nm (Fig. 1 B). We characterized the calibration procedure by doing a systematic variation of the spot diameter, the number of spots, and the central position of the calibration pattern (see Fig S8). Increasing the number of spots across the field of view will constrain the transformation more, potentially resulting in a better fit. However, in practice, the increased density of spots increases the background intensity and is more likely to result in mistakes in the automated segmentation and sorting while not offering much improvement in accuracy.

FRAP

A 488 nm laser at a power density of 1.7 W/cm^2 was used to excite GFP in the full field of view for 2 seconds (Fig. 2 A, left). The averaged frames over this time were used to select regions of the ER in each cell to generate a DMD mask for bleaching (Fig. 2 A, second from left). The selected spots were bleached for 60s at a power density of 89 W/cm^2 (Fig. 2 A, center). To minimize bleaching while measuring the fluorescence recovery, the full field of view was subsequently illuminated with a 488 nm laser pulse with a duration of 0.2 seconds repeated every second at a power density of 1.7 W/cm^2. To determine the ROI for measuring fluorescence recovery, a subset of the frames during bleaching were averaged in

time and a maximum entropy threshold [33] was applied to the fluorescence image in Fiji. The intersection of the resulting area with the DMD mask was used to measure bleaching and recovery of fluorescence (Fig. 2 A, second from right and right).

To correct for overall bleaching of the sample during the recovery measurement, which was measured to be less than 5%, each frame was normalized by the mean intensity of the pre-bleaching frames. Another region outside the cells but close to the bleached region was selected as a background measurement. Using these regions, the bleach-corrected normalized mean intensity of the bleached region, $I(t)$, was calculated as

$$I(t) = \frac{I_{\text{dmd}}(t) - I_{\text{bg}}(t)}{\overline{I_{\text{bmd}}(t < 0)} - \overline{I_{\text{bg}}(t < 0)}} \qquad (2)$$

where $I_{\text{dmd}}(t)$ is the spatial average of the bleach-corrected intensity of the bleached region, $I_{\text{bg}}(t)$ is the spatial average of the bleach-corrected intensity of the background region near the ER but where no cells were present. $t < 0$ indicates the pre-bleaching frames, and the overbar indicates a time-average of the spatially-averaged intensities before bleaching. The recovery curve was fit to the model for a circular bleaching spot with a rectangular profile [34] (Fig. 2 B)

$$I(t) = I_0 + (I_{\text{inf}} - I_0)e^{-2\tau/t}(J_0(2\tau/t) + J_1(2\tau/t)) \qquad (3)$$

where I_0 is the fluorescence intensity immediately after bleaching, I_{inf} is the fluorescence intensity long after recovery, J_0 and J_1 are the zeroth and first Bessel functions, respectively, and τ is the characteristic diffusion time, $\tau = w^2/4D$, where w is the radius of the bleaching spot and D is the diffusion coefficient.

PALM

CF488 was excited by 488 nm at 0.45 W/cm^2 for 1 second to find the PM of cells and to draw a mask for patterned photoactivation (Fig 3 A, B and C). A patterned 405 nm laser was used to photoconvert mEos2 from the green state to the red state and a 561 nm laser was used to excite mEos2 in its red state (Fig 3 A and B). The illumination sequence consisted of one frame of 405 nm photoactivation with increasing power followed by nine frames of 561 nm excitation at a framerate of 20 Hz for up to 40,000 frames. Every 100 frames the 405 nm photoactivation frame was replaced by low power 488 nm excitation to potentially prolong the mEos2 trace lengths [35] and to potentially detect an increase in autofluorescence.

Single-molecule localization microscopy (SMLM) analysis was performed using Insight3 software (Zhuang lab, Harvard) (Fig. 3 D, E and F). Single-molecule recognition was confirmed by visual perception of fluorescent blinking and single-molecule identification parameters for 2D Gaussian point-spread functions (PSFs) were set accordingly (Gaussian height 47 photons, width 280–750 nm, ROI: 7×7 pixels). All single-molecule localizations were rendered as uniform Gaussian peaks. All super-resolution images were represented across at least 36,000 frames at 20 Hz, corresponding to 1,800 seconds (Fig. 3 F and S7).

To account for differences in the initial intensity of each cell, the average intensity during the first 2001 frames was subtracted from the mean intensity trace of each cell (Fig 3 G).

The mean cumulative counts were calculated by using the ROIs around each cell for measuring the mean intensity but excluding the cytoplasmic background localizations that are more dominant in fully photoactivated cells. We then averaged the cumulative counts of localizations per cell at each frame across all fully and partially photoactivated cells (Fig. 3 H and I).

Since SMLM cannot be reliably performed when the background intensity of cells increases due to phototoxic effects, we determined a single cutoff intensity for all cells, at which the false positive rate of single-molecule localizations became excessive and at which cells transitioned to an unhealthy state. We determined the cutoff intensity change (56 counts) from a single movie by averaging the intensity change of three partially photoactivated cells with the lowest intensity in the last frame. Single-molecule localizations were considered invalid after the time at which each cell's mean intensity change exceeded the cutoff intensity of 56 counts (Fig. 3 G, H, I and S4).

Single-molecule traces were made from localizations before the cutoff time. Using custom software written in MATLAB (The MathWorks, Natick, MA), single-molecule localizations were linked within a radius of 0.9 μm and only traces with a length of at least 3 frames (0.15 seconds) were used for further analysis (Fig 4).

To determine the diffusion coefficient, D, of mEos2 fused to the PH-domain of Plc(delta1) in fully and partially illuminated cells, we calculated the average mean squared displacement (MSD) from single-molecule traces by averaging over all squared displacements at each lag time, t. In the case of normal diffusion in two dimensions, the MSD is linear in time. We obtained D by fitting the MSD data to the model [36] (Fig. 4 B)

$$\mathrm{MSD}(\Delta t) = 4D\Delta t + 2\sigma^2 \tag{5}$$

where σ is the uncertainty in position [36,37].

Results and discussion

Computer-based calibration of a DMD allows for spatial light modulation with precision below the optical diffraction limit

A general challenge for precisely modulating light in the sample plane of a microscope is to map the pixels of the DMD to the camera pixels. While linear offsets in the sample plane can be manually corrected by adjustments, nonlinear distortions caused by the optical components in the laser path remain to be a source of misalignment. This misalignment hinders the ability to confine illumination to only regions of a cell where fluorescent probes are located while reducing unnecessary illumination that would contribute to phototoxicity. Here, we develop a fast and simple computer-based calibration procedure, which accounts for both, translational misalignments as well as nonlinear distortions. First, a regular pattern of equally spaced spots is projected in the sample plane and the resulting fluorescence image is recorded with the camera. Next, the transformation between the coordinate system of the

DMD and the sample plane is determined by fitting a 3rd-order polynomial to the centers of the spots. By applying the inverse transformation to any arbitrary pattern, all offsets and distortions are corrected, and the DMD and camera coordinate system are matched (see also Materials and Methods, Fig. 1 and Fig. S2).

We performed the calibration by projecting a 4×4 grid of spots, each with a diameter of 1.83 μm and a 9.53 μm center-to-center spacing, onto a layer of fluorescein dye solution in the sample plane (Fig. 1 A and Fig. S2). The projected pattern covered most of the field of view, which we restricted to 256×256 camera pixels, or 41×41 $μm^2$. After determining the centroids of these spots by fitting each to a Gaussian profile, we calculated the inverse transformation that returns the original projected pattern. The 16 points were fit to a 3rd-order polynomial in two variables (20 parameters, see Eq. 1 and Materials and Methods). To demonstrate the advantage of our computer-based calibration we simulated a manual adjustment of the DMD by only allowing a rigid transformation – translation, scaling, and rotation about the beam axis – which are the degrees of freedom that could be optimized by manual alignment. This transformation resulted in a significant discrepancy since it cannot correct nonlinear distortions of the optical system (Fig. 1 B). By calibrating with our computer-based approach and allowing shear degrees of freedom in the 1st-order and curved lines in higher orders of the transformation, in the 3rd-order transformation (Fig. 1 B and Fig. S2), we achieve a median deviation within the optical diffraction limit and on the order of the single-molecule localization precision, which is tens of nanometers [7–10]. Computer-based calibration with a nonlinear transformation is not only more precise than a rigid transformation achievable by a manual calibration but is also a fast and convenient way to account for small changes in the alignment of optical components. Performing a calibration before each experiment can be done in a total of less than twenty minutes including instrument startup and dye preparation. These results demonstrate that our computer-based DMD calibration is an easy and fast approach to precisely match the coordinate system of the DMD and the camera to accurately illuminate multiple regions across the field of view for advanced fluorescence microscopy applications with patterned illumination.

Application of a calibrated DMD to Fluorescence Recovery after Photobleaching experiments

As a demonstration of this system's accuracy for conventional microscopy applications, we performed a fluorescence recovery after photobleaching (FRAP) experiment with GFP fused to IRE1, which localizes to the endoplasmic reticulum (ER) of *S. cerevisiae*. In a FRAP experiment, a conventional fluorescence image is taken first to record the spatial distribution of the labeled molecules and to select a small region for photobleaching using a high-powered laser. A well calibrated DMD is therefore critical to precisely define the region of interest (ROI) for bleaching. This photobleaching is followed by a low-powered laser excitation of the entire field of view to measure the fluorescence recovery in the bleached region while the fluorescent membrane-bound molecules diffuse back. The diffusion coefficient of the mobile species present in the membrane can then be derived from the rate of fluorescence recovery and the fraction of mobile species can be determined from the steady-state intensity of the ROI after bleaching was applied.

When the diffusing protein, IRE1-GFP, was excited with a 488 nm laser at low power, the detected fluorescence signal showed the expected outline of the ER around the nucleus and in proximity to the plasma membrane of the yeast cells (Fig. 2 A, left). Due to the precise calibration of the DMD, the recorded fluorescence image allowed us to select a small region for bleaching on the DMD (Fig. 2 A, second from left). During bleaching, only the selected region of the DMD was turned on and the resulting bright fluorescence caused by the high excitation power confirmed the accuracy of the DMD calibration (Fig. 2 A, center, and Fig. S3). Due to the extension of the selected spot beyond the ER of the cell and due to optical diffraction, the shape of the fluorescent signal is not identical to the selected region. After bleaching the selected region, the entire field of view was excited again at low laser power to monitor the fluorescence recovery in the bleached region (Fig. 2 A, second from right and right). The normalized and bleach-corrected intensity of the fluorescence recovery curve in the region of the cell outlined in red (Fig. 2 A, second from right and right) allowed us to determine the diffusion coefficient of IRE1-GFP in the ER by fitting the model in Eq. 3 (Fig. 2 B). Based on the model, the diffusion coefficient was determined to be $0.00276 \pm 0.00018 \ \mu m^2/s$ with a mobile fraction of 89%. These results demonstrate that our calibration procedure enables accurate selection of regions from a fluorescence microscopy image for FRAP experiments.

Spatially informed photoactivation enables longer imaging times in single-molecule localization microscopy with an improved number of localizations

One challenge in SMLM is the long imaging time caused by the requirement for sparse photoactivation and the need to acquire enough single-molecule localizations to fulfill the Nyquist criterion for resolving a cellular structure. In addition, imaging for a long time can be necessary for studying dynamic processes in live cells such as observing the time evolution of intracellular signals or organelle trafficking. A major problem associated with long imaging times is the exposure of cells to the high energy photons from the 405 nm photoactivation laser, which causes phototoxicity in all cell types [38–40]. Here we employ our calibrated DMD to develop a spatially informed illumination approach for photoactivation, which reduces phototoxic effects, results in more localizations compared to traditional photoactivation and extends the viable SMLM imaging time. In this approach a conventional fluorescence image is acquired to record the diffraction-limited spatial distribution of a protein localized to the cellular structure of interest. Next, this image is used to create a binary mask on the DMD and to expose only those regions within cells to 405 nm photoactivating light where the proteins of interest are located and to avoid unnecessarily exposing other regions of the cell. In order to keep the photoactivation mask as small as possible and to accurately photoactivate the selected region, a calibration of the DMD with a precision below the optical diffraction limit is needed as described previously. The entire field of view is then excited for nine frames with 561 nm light to image and localize single molecules. This cycle of spatially patterned photoactivation and excitation is repeated thousands of times until all labeled proteins are activated and imaged.

As a model system to demonstrate spatially informed photoactivation for SMLM we used an *S. cerevisiae* strain in which the plasma membrane (PM) localizing PH domain of Plc(delta1) fused to the photoactivatable fluorescent protein (PAFP) mEos2 is expressed at

low levels. While in principle the green pre-activated state of mEos2 could be used to create a conventional fluorescence image for the patterned photoactivation mask, we stained the cell wall in addition with fluorescently-labeled ConA, which is excited with low power of 488 nm light. This additional staining increases the fluorescence signal from the proximity of the PM and decreases bleaching of pre-activated mEos2 by requiring lower excitation powers. First, we excited the fluorescently-labeled ConA with a low power of 488 nm light and recorded a conventional fluorescence image of cells to create a photoactivation mask around the entire cell as a control for conventional PALM (Fig. 3 A and B, upper). Next, the mask was transformed with the inverse transformation between the camera and DMD coordinate system as previously described in the Material and Methods. A PALM data acquisition sequence consisting of one frame of 405 nm photoactivation followed by nine frames of 561 nm excitation for up to 2000 seconds. Every 100 frames the 405 nm photoactivation frame was replaced by low power 488 nm excitation to potentially prolong the trace lengths [35] and potentially detect an increase in autofluorescence. During the 561 nm excitation frames, initially single mEos2 molecules became visible at the PM (Fig. 3 D, upper) and were fitted to determine their precise location. However, after longer data acquisition, the autofluorescence of the cells started to increase, which indicated phototoxic effects [41](Fig. 3 E, upper). Localizations recorded after this transition to an unhealthy cell state were considered unreliable because of the cell's altered physiological state and because of the high fluorescence background. After even longer imaging times, the cell's morphology was altered (shrinking) and only bright autofluorescence was falsely detected and fitted as single molecules (Fig. 3 E, upper). The rendered super-resolution image in Fig. 3 F, upper, shows the expected outline of the PM for localizations before the transition to the unhealthy state (green). After the transition to an unhealthy state and the change in cell morphology only false localizations were detected inside the original outline of the PM (red squares in Fig. 3 E, upper).

In the same PALM movies, we selected cells for spatially informed photoactivation (Fig. 3 A, lower). A mask for photoactivation was created only around the PM of these cells where the PH-mEos2 protein is localized, leaving a region inside the cell without 405 nm light exposure (Fig 3 B, lower). The same PALM imaging sequence was used as before, and single molecules were fitted (Fig. 3 D and E, lower) and rendered in a super-resolution image (Fig. 3 F, lower). In strong contrast to the fully photoactivated cells, the partially activated cell did not show any signs of phototoxicity after long imaging times and only some cells exhibited a slow increase autofluorescence towards the end of the PALM movie. Therefore, more reliable localizations were detected, and false positive localizations were almost negligible. Almost all localizations from the cell in Fig. 3 F, lower, show the PM localizations as expected and due to the longer imaging time contains more dense localizations compared to the fully activated cell in Fig. 3 F, upper.

To define the transition of each cell to an unhealthy state, we plotted their mean intensity change when excited with 561 nm light (Material and Methods and Fig. S4). As can be seen in Fig. 3 G, the mean intensity change of fully activated cells consistently increases after the transition from a healthy to an unhealthy state. The same trend can be seen in mean the cumulative number of localizations per cell (Fig. 3 H), which only contain false positives after the transition to an unhealthy state due to the bright fluorescence background.

For each cell, we then defined the transition to a noticeable change in mean background fluorescence to be 56 counts (Fig. 3 G and S4 and Materials and Methods). While this threshold is somewhat arbitrary, it is the lowest that is visually noticeable in each frame and above the noise of the mean intensity vs. time traces of each cell (Fig. S4 A). Furthermore, this threshold can be consistently applied to all fully and partially photoactivated cells. From the single-molecule data, fully illuminated cells showed an average increase in background of 121% after their respective cutoff times while partially illuminated cells only showed only a 47% increase (Fig. S5). The increase in autofluorescence background of fully illuminated cells therefore not only reports on the altered physiological state and morphological change of cells but also causes a high false positive rate of localizations and a high background level in those localizations (Fig. S5 and Fig. S7).

As indicated in Fig. 3 F and G, the mean time to reach an unhealthy state for partially photoactivated cells was 44% longer compared to fully activated cells and some partially activated cells even did not reach this state within the imaging time of 2000 seconds. We note that the mean intensity at the mean transition time for fully activated cells is lower compared to partially activated cells because some partially activated cells did not reach the intensity threshold within the imaging time. These results demonstrate that spatially informed photoactivation allows for significantly longer imaging times by decreasing phototoxicity. Importantly, this extended imaging time also significantly increases the number of localizations per cell and thus the quality of super-resolution images. By determining the number of localizations per cell until the transition to an unhealthy state, we found a significant 28% increase in the mean number of localizations from partially activated cells compared to fully activated cells (Fig. 3 I). While the distribution of the number of localizations is broad compared to fully activated cells, this result shows the recording SMLM data with spatially informed photoactivation increases detected localizations and improves the quality of super-resolution data.

Spatially informed photoactivation results in the same localization precision and improved ability for single-molecule tracking

SMLM yields quantitative information of the spatial organization of single molecules. By linking localizations from the same molecule in subsequent frames, single-molecules can be tracked and valuable and complementing information about the dynamics of single molecules is obtained such as their diffusion coefficients and differences in mobility or transport modes [42,43]. The diffusion of a molecule can reveal information about interactions with a binding partner or if there are different subpopulations of the molecules within a cell [44,45]. Just as a larger number of localizations is beneficial for SMLM, an increased number of single molecule traces is desired to obtain higher statistics for calculating diffusion coefficients and for discriminating different subpopulations.

To verify that spatially informed photoactivation does not alter the localization precision or the accuracy of single-molecule tracking compared to traditional SMLM, we performed single-molecule tracking experiments with the same 2xPH-domain fused to mEos2 under partial and full photoactivation conditions. For both imaging modes, single-molecule traces were created by linking localizations that appeared within 0.9 μm and within 1 frame (see

Materials and Methods). Given our average photoactivation density of 0.003 localizations per frame and per μm^2, the probability for accidentally linking two separate molecules is less than 0.3%.

Under both, full and partial photoactivation, we observed the expected traces of single molecules along the plasma membrane of yeast cells (Fig. 4 A). To further analyze the diffusion of molecules, we calculated the mean square displacement of traces from fully and partially photoactivated cells and fitted the linear model of Eq. 5 (see Materials and Methods). The resulting diffusion coefficients for full and partial photoactivation agreed within the error of the experiment (Fig 4B). Since the length of single-molecule traces affects the accuracy of determining diffusion coefficients, we compared the histograms of trace lengths under full and partial photoactivation and did not detect significant differences (Fig. 4 C).

In SMLM, a larger number of photons emitted by a single emitter increases the localization precision as $\sigma \sim 1/\sqrt{N}$ [46]. We therefore compared the photon statistics of reliable localizations for full and partial photoactivation. Again, no significant difference in the mean number of photons between fully and partially illuminated cells was detected (Fig. 4D). These results demonstrate that spatially informed photoactivation has no effect on the ability to accurately localize single molecules and to study their diffusion in SMLM applications. The increase in imaging time due to reduction of phototoxicity as well as the increased number of reliable localizations therefore presents a significant advantage of spatially informed photoactivation compared to traditional photoactivation of an entire cell. Our simple and precise calibration approach for patterned illumination applications as well as the development of spatially informed photoactivation will therefore become of broad applicability that extends far beyond the proof of concept of this work.

Conclusions

In this work we presented a fast, easy and accurate approach to calibrate DMDs for patterned illumination applications in fluorescence microscopy. Our computer-based transformation between the camera and DMD coordinate system replaces the need for small manual adjustments and results in an improved accuracy within the diffraction limit due to the additional nonlinear degrees of freedom of the transformation that cannot be simultaneously optimized otherwise. We demonstrated the usefulness of this approach in a conventional FRAP experiment with the ER localized protein IRE1 fused to GFP. Furthermore, we employed the precise calibration of the DMD to develop a novel, spatially informed photoactivation approach for SMLM. In this approach only regions within the cell are exposed to 405 nm light in which photoswitchable fluorescent proteins are located. To accurately photoactivate the selected structure while keeping the photoactivation mask as small as possible, calibration of the DMD with a precision below the optical diffraction is required. As a result, the possible imaging time until signs of phototoxicity were detected increased by 44% and 28% more single-molecule localizations were recorded. Spatially informed photoactivation results in the same localization precision and thus improves single-molecule tracking since more single molecule traces are detected. Therefore, spatially informed photoactivation presents a significant improvement of SMLM

experiments compared to the traditional photoactivation of the entire field of view and will enable a myriad of applications in quantitative cell biology to study cellular processes and structures below the optical diffraction limit.

Supplementary Material

Refer to Web version on PubMed Central for supplementary material.

Acknowledgements

References

[1]. Axelrod D, Koppel DE, Schlessinger J, Elson E and Webb WW 1976 Mobility measurement by analysis of fluorescence photobleaching recovery kinetics. Biophys J 16 1055–69 [PubMed: 786399]

[2]. Hoebe RA, Oven CHV, Jr T W J G, Dhonukshe PB, Noorden CJFV and Manders EMM 2007 Controlled light-exposure microscopy reduces photobleaching and phototoxicity in fluorescence live-cell imaging Nature Biotechnology 25 249–53

[3]. Chu KK, Lim D and Mertz J 2007 Enhanced weak-signal sensitivity in two-photon microscopy by adaptive illumination Optics Letters 32 2846 [PubMed: 17909593]

[4]. Banghart M, Borges K, Isacoff E, Trauner D and Kramer RH 2004 Light-activated ion channels for remote control of neuronal firing Nature Neuroscience 7 1381–6 [PubMed: 15558062]

[5]. Nagel G, Szellas T, Huhn W, Kateriya S, Adeishvili N, Berthold P, Ollig D, Hegemann P and Bamberg E 2003 Channelrhodopsin-2, a directly light-gated cation-selective membrane channel Proceedings of the National Academy of Sciences 100 13940–5

[6]. Levskaya A, Weiner OD, Lim WA and Voigt CA 2009 Spatiotemporal control of cell signalling using a light-switchable protein interaction. Nature 461 997–1001 [PubMed: 19749742]

[7]. Rust MJ, Bates M and Zhuang X 2006 Sub-diffraction-limit imaging by stochastic optical reconstruction microscopy (STORM) Nature Methods 3 793–6 [PubMed: 16896339]

[8]. Betzig E, Patterson GH, Sougrat R, Lindwasser OW, Olenych S, Bonifacino JS, Davidson MW, Lippincott-Schwartz J and Hess HF 2006 Imaging Intracellular Fluorescent Proteins at Nanometer Resolution Science 313 1642–5 [PubMed: 16902090]

[9]. Klar TA, Jakobs S, Dyba M, Egner A and Hell SW 2000 Fluorescence microscopy with diffraction resolution barrier broken by stimulated emission PNAS 97 8206–10 [PubMed: 10899992]

[10]. Hell SW and Wichmann J 1994 Breaking the diffraction resolution limit by stimulated emission: stimulated-emission-depletion fluorescence microscopy Optics Letters 19 780 [PubMed: 19829529]

[11]. Puchner EM, Walter JM, Kasper R, Huang B and Lim WA 2013 Counting molecules in single organelles with superresolution microscopy allows tracking of the endosome maturation trajectory Proc. Natl. Acad. Sci. U.S.A 110 16015–20 [PubMed: 24043832]

[12]. Annibale P, Vanni S, Scarselli M, Rothlisberger U and Radenovic A 2011 Identification of clustering artifacts in photoactivated localization microscopy Nat Meth 8 527–8

[13]. Durisic N, Laparra-Cuervo L, Sandoval-Álvarez A, Borbely JS and Lakadamyali M 2014 Single-molecule evaluation of fluorescent protein photoactivation efficiency using an in vivo nanotemplate Nat. Methods 11 156–62 [PubMed: 24390439]

[14]. Dickson RM, Cubitt AB, Tsien RY and Moerner WE 1997 On/off blinking and switching behaviour of single molecules of green fluorescent protein Nature 388 355–8 [PubMed: 9237752]

[15]. Schwartz SL, Yan Q, Telmer CA, Lidke KA, Bruchez MP and Lidke DS 2015 Fluorogen-Activating Proteins Provide Tunable Labeling Densities for Tracking FcɛRI Independent of IgE ACS Chemical Biology 10 539–46 [PubMed: 25343439]

[16]. Smith EM, Gautier A and Puchner EM 2019 Single-Molecule Localization Microscopy with the Fluorescence-Activating and Absorption-Shifting Tag (FAST) System ACS Chemical Biology 14 1115–20 [PubMed: 31083964]

[17]. Valiya Peedikakkal L, Steventon V, Furley A and Cadby AJ 2017 Development of targeted STORM for super resolution imaging of biological samples using digital micromirror device Optics Communications 404 18–22

[18]. Chen S-Y, Bestvater F, Schaufler W, Heintzmann R and Cremer C 2018 Patterned illumination single molecule localization microscopy (piSMLM): user defined blinking regions of interest Opt. Express, OE 26 30009–20

[19]. Chakrova N, Rieger B and Stallinga S 2015 Development of a DMD-based fluorescence microscope ed Brown TG, Cogswell CJ and Wilson T p 933008

[20]. Zhu P, Fajardo O, Shum J, Zhang Schärer Y-P and Friedrich RW 2012 High-resolution optical control of spatiotemporal neuronal activity patterns in zebrafish using a digital micromirror device Nature Protocols 7 1410–25 [PubMed: 22743832]

[21]. Dan D, Lei M, Yao B, Wang W, Winterhalder M, Zumbusch A, Qi Y, Xia L, Yan S, Yang Y, Gao P, Ye T and Zhao W 2013 DMD-based LED-illumination Super-resolution and optical sectioning microscopy Scientific Reports 3

[22]. Liang CW, Mohammadi M, Santos MD and Tang C-M 2011 Patterned Photostimulation with Digital Micromirror Devices to Investigate Dendritic Integration Across Branch Points Journal of Visualized Experiments

[23]. Lubeck E and Cai L 2012 Single-cell systems biology by super-resolution imaging and combinatorial labeling Nat Methods 9 743–8 [PubMed: 22660740]

[24]. Bianchi F, Syga Ł, Moiset G, Spakman D, Schavemaker PE, Punter CM, Seinen A-B, van Oijen A M, Robinson A and Poolman B 2018 Steric exclusion and protein conformation determine the localization of plasma membrane transporters Nat Commun 9 1–13 [PubMed: 29317637]

[25]. Mund M, van der Beek J A, Deschamps J, Dmitrieff S, Hoess P, Monster JL, Picco A, Nédélec F, Kaksonen M and Ries J 2018 Systematic Nanoscale Analysis of Endocytosis Links Efficient Vesicle Formation to Patterned Actin Nucleation Cell 174 884–896.e17 [PubMed: 30057119]

[26]. Adhikari S, Moscatelli J, Smith EM, Banerjee C and Puchner EM 2019 Single-molecule localization microscopy and tracking with red-shifted states of conventional BODIPY conjugates in living cells Nat Commun 10 1–12 [PubMed: 30602773]

[27]. Longtine MS, McKenzie A, Demarini DJ, Shah NG, Wach A, Brachat A, Philippsen P and Pringle JR 1998 Additional modules for versatile and economical PCR-based gene deletion and modification in Saccharomyces cerevisiae Yeast 14 953–61 [PubMed: 9717241]

[28]. Pincus D, Chevalier MW, Aragón T, van Anken E, Vidal SE, El-Samad H and Walter P 2010 BiP binding to the ER-stress sensor Ire1 tunes the homeostatic behavior of the unfolded protein response PLoS Biol 8 e1000415 [PubMed: 20625545]

[29]. Chau AH, Walter JM, Gerardin J, Tang C and Lim WA 2012 Designing synthetic regulatory networks capable of self-organizing cell polarization Cell 151 320–32 [PubMed: 22727045]

[30]. Puchner EM, Walter JM, Kasper R, Huang B and Lim W a 2013 Counting molecules in single organelles with superresolution microscopy allows tracking of the endosome maturation trajectory. Proceedings of the National Academy of Sciences of the United States of America 110 16015–20 [PubMed: 24043832]

[31]. Bradski, G; The OpenCV Library. Dr. Dobb's Journal of Software Tools. 2000.

[32]. van der Walt S, Schönberger JL, Nunez-Iglesias J, Boulogne F, Warner JD, Yager N, Gouillart E and Yu T 2014 scikit-image: image processing in Python PeerJ 2 e453 [PubMed: 25024921]

[33]. Sahoo PK, Soltani S and Wong AKC 1988 A survey of thresholding techniques Computer Vision, Graphics, and Image Processing 41 233–60

[34]. Soumpasis DM 1983 Theoretical analysis of fluorescence photobleaching recovery experiments Biophys. J 41 95–7 [PubMed: 6824758]

[35]. De Zitter E, Thédié D, Mönkemöller V, Hugelier S, Beaudouin J, Adam V, Byrdin M, Van Meervelt L, Dedecker P and Bourgeois D 2019 Mechanistic investigation of mEos4b reveals a strategy to reduce track interruptions in sptPALM Nature Methods

[36]. Martin DS, Forstner MB and Käs JA 2002 Apparent Subdiffusion Inherent to Single Particle Tracking Biophysical Journal 83 2109–17 [PubMed: 12324428]

[37]. Dietrich C, Yang B, Fujiwara T, Kusumi A and Jacobson K 2002 Relationship of Lipid Rafts to Transient Confinement Zones Detected by Single Particle Tracking Biophysical Journal 82 274–84 [PubMed: 11751315]

[38]. Wäldchen S, Lehmann J, Klein T, van de Linde S and Sauer M 2015 Light-induced cell damage in live-cell super-resolution microscopy Scientific Reports 5 15348 [PubMed: 26481189]

[39]. Laissue PP, Alghamdi RA, Tomancak P, Reynaud EG and Shroff H 2017 Assessing phototoxicity in live fluorescence imaging Nature Methods 14 657–61 [PubMed: 28661494]

[40]. Icha J, Weber M, Waters JC and Norden C 2017 Phototoxicity in live fluorescence microscopy, and how to avoid it BioEssays 39 1700003

[41]. Surre J, Saint-Ruf C, Collin V, Orenga S, Ramjeet M and Matic I 2018 Strong increase in the autofluorescence of cells signals struggle for survival Sci Rep 8 1–14 [PubMed: 29311619]

[42]. Manley S, Gillette JM, Patterson GH, Shroff H, Hess HF, Betzig E and Lippincott-Schwartz J 2008 High-density mapping of single-molecule trajectories with photoactivated localization microscopy Nature Methods 5 155–7 [PubMed: 18193054]

[43]. Kapanidis AN, Uphoff S and Stracy M 2018 Understanding Protein Mobility in Bacteria by Tracking Single Molecules Journal of Molecular Biology 430 4443–55 [PubMed: 29753778]

[44]. Knight SC, Xie L, Deng W, Guglielmi B, Witkowsky LB, Bosanac L, Zhang ET, Beheiry ME, Masson J-B, Dahan M, Liu Z, Doudna JA and Tjian R 2015 Dynamics of CRISPR-Cas9 genome interrogation in living cells Science 350 823–6 [PubMed: 26564855]

[45]. Martens KJA, van Beljouw SPB, van der Els S, Vink JNA, Baas S, Vogelaar GA, Brouns SJJ, van Baarlen P, Kleerebezem M and Hohlbein J 2019 Visualisation of dCas9 target search in vivo using an open-microscopy framework Nature Communications 10

[46]. Thompson RE, Larson DR and Webb WW 2002 Precise nanometer localization analysis for individual fluorescent probes. Biophys J 82 2775–83 [PubMed: 11964263]

[47]. Brown DC. 1966; Decentering Distortion of Lenses. Photogrammetric Engineering. 19

[48]. Zhang Z 2000 A flexible new technique for camera calibration IEEE Trans. Pattern Anal. Machine Intell 22 1330–4

[49]. Ho J, Tumkaya T, Aryal S, Choi H and Claridge-Chang A 2019 Moving beyond P values: data analysis with estimation graphics Nature Methods 16 565 [PubMed: 31217592]
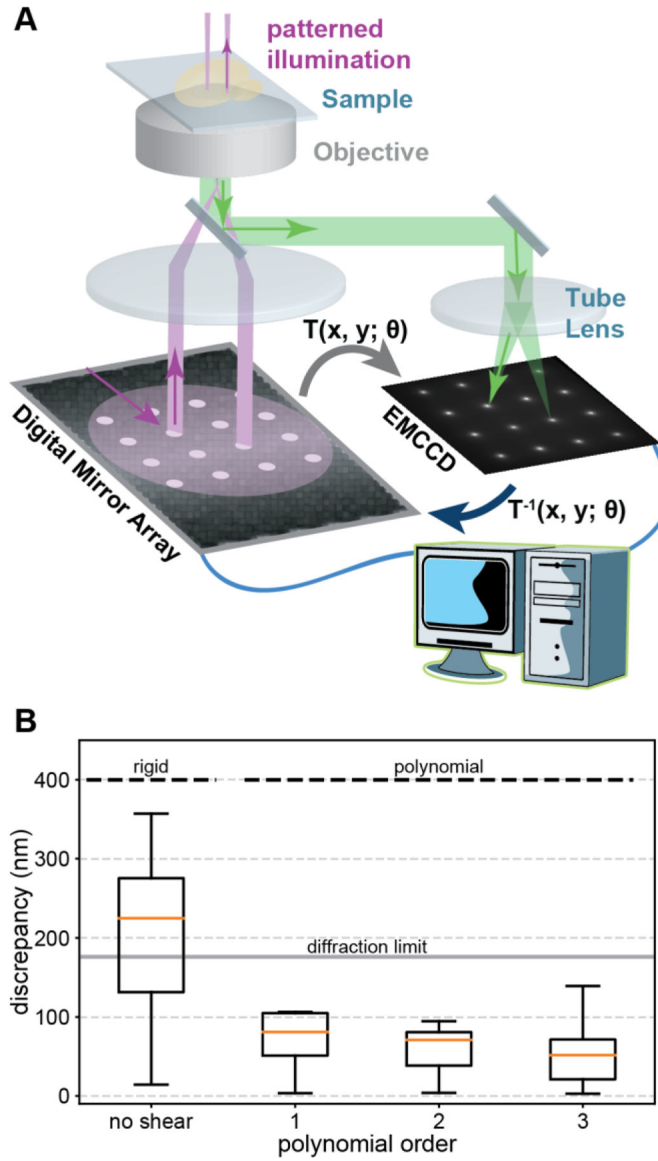
Figure 1: Schematics of spatially informed illumination setup and calibration.
(A) A digital micromirror device is mounted in the excitation path of a PALM microscope.
Pixels in the on state reflect laser light, which gets projected onto the back focal
plane of the microscope objective (purple, 4F lens system not shown for clarity). The
fluorescence (green) of the calibration pattern of 4×4 spots is recorded with the camera
and the transformation T between the DMD and camera coordinate system is determined
with a computer to correct for rigid and higher order polynomial distortions caused by
optical components [47,48]. (B) Varying degrees of freedom are included in the inverse
transformation T^{-1} of the calibration pattern to correct for distortions. (Left) Rigid degrees
of freedom simulating a perfect manual alignment result in a significant median discrepancy
above the theoretical diffraction limit of the emission peak of fluorescein. (Right) Including
higher order polynomials in T^{-1} results in an accurate matching of the DMD and camera
coordinate system with a median discrepancy well below the diffraction limit. Boxes extend

from the 25th to 75th percentiles (interquartile range, IQR). Medians are shown as orange horizontal lines. Whiskers extend to the farthest data point within 1.5 IQR below and above the 25th and 75th percentiles, respectively.
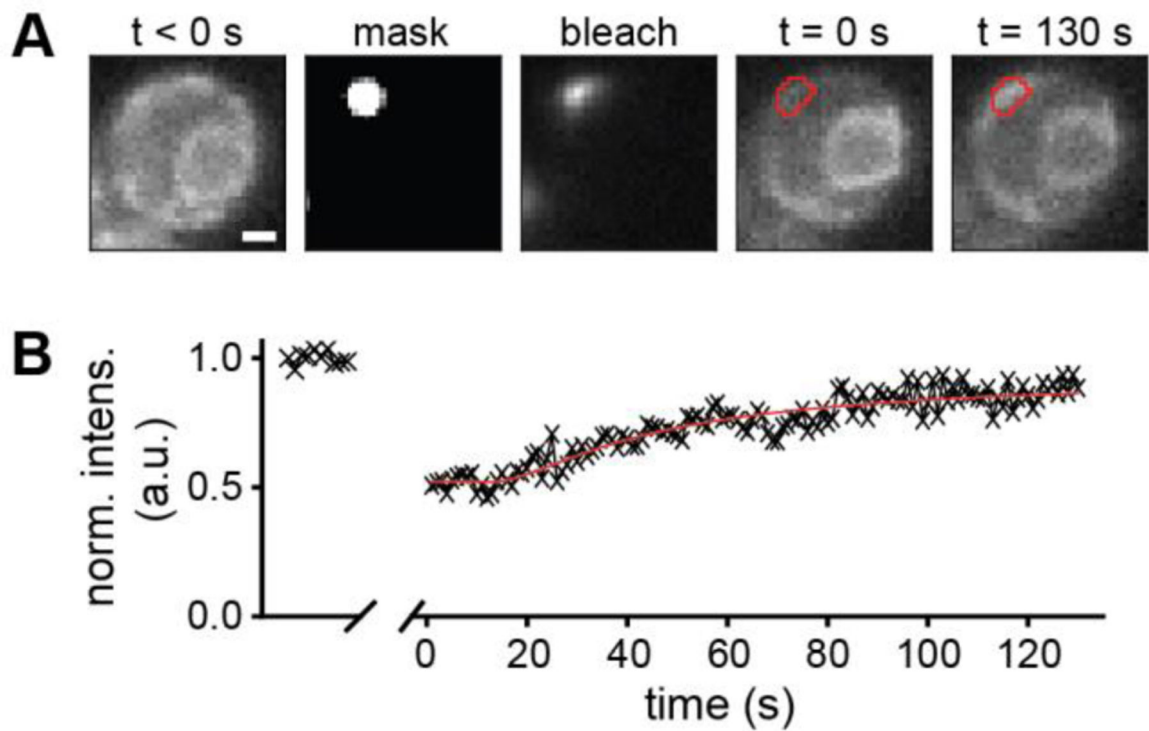
Figure 2: Proof of concept FRAP experiment.
(A, left) Fluorescence image of IRE1-GFP before bleaching. (A, second from left) Selected spot for bleaching IRE1-GFP with 488 nm light. (A, center) Fluorescence of IRE1-GFP during bleaching. (A, second from right) Fluorescence image of IRE1-GFP after bleaching of the selected spot (red outline). (A, right) Fluorescence image of IRE1-GFP after fluorescence recovery of the selected spot (red outline) (B) Normalized bleach-corrected intensity of the IRE1-GFP emission within the bleached region outlined in red. Scale bar: 1 μm.
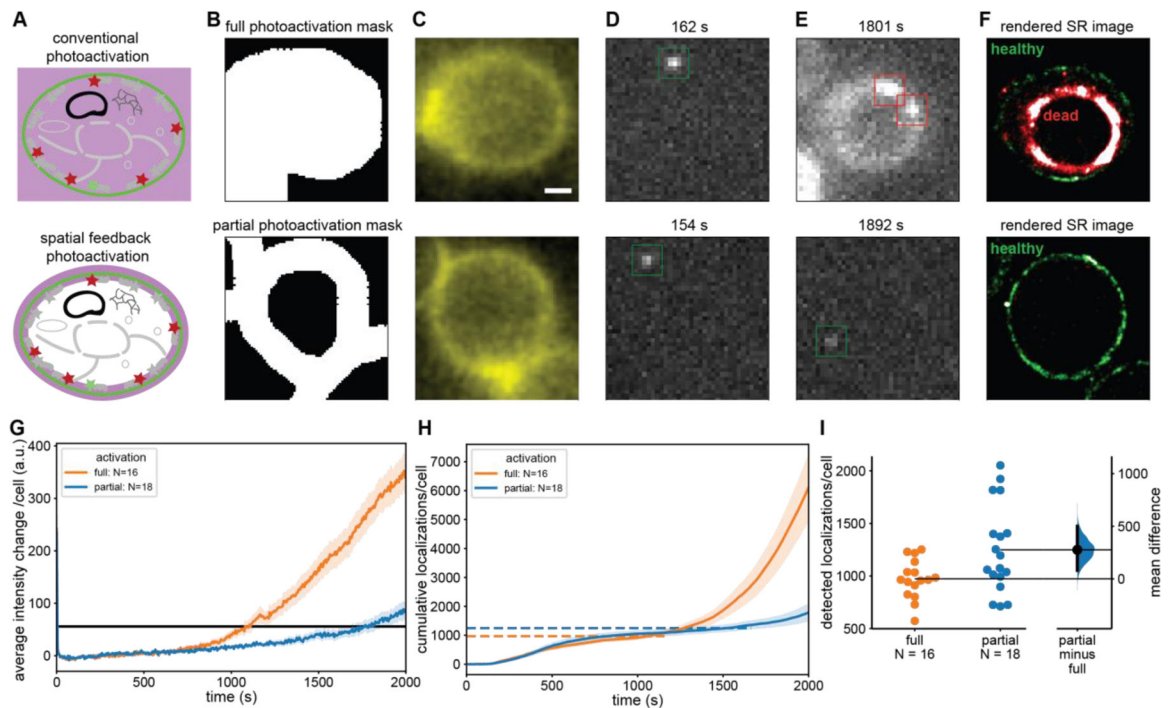
Figure 3: Spatially informed photoactivation significantly improves SMLM image quality through an increased number of localizations.

(A) In conventional PALM the entire cell is exposed to 405 nm photoactivation light (upper) whereas in spatially informed PALM only the regions that contain PAFPs are photoactivated (lower). (B) A mask is selected covering the entire cell (upper) and another mask which excludes the cytoplasm covering only the PM where mEos2 is located (lower). (C) Fluorescence image of CF488M conjugated to ConA excited at 488 nm used to create the mask in (B). (D, E) Individual frames with single-molecule localizations of mEos2 under 561 nm excitation at early (D) and late (E) timepoints during PALM data acquisition. The fully illuminated cell shows signs of phototoxicity including autofluorescence much sooner (upper) than the partially illuminated cells (lower). (F) Rendered PALM image showing mEos2 localizations while cells are healthy (green) and after the transition to the unhealthy state (red). (G) Mean autofluorescence intensity change of fully and partially illuminated cells (orange and blue respectively) under 561 nm excitation and cutoff for transition to unhealthy state (black line). (H) Mean cumulative localizations of fully and partially illuminated cells (orange and blue, respectively) with horizontal dashed lines showing the mean number of localizations at the cutoff time. Localizations after the transition to the unhealthy state are unreliable and predominantly caused by autofluorescence. (I) Gardner-Altman plot of the total number of localizations from fully and partially illuminated cells up to transition to unhealthy state compared at the 95% confidence interval. (Mann-Whitney $p < 0.05$) [49] A significant 28% increase in reliable mEos2 localizations is detected in spatially informed PALM compared to conventional PALM. Error bands: standard error of the mean across cells. Top and bottom of B, C, D, E, and F are the same scale. Scale bar is 1 µm.
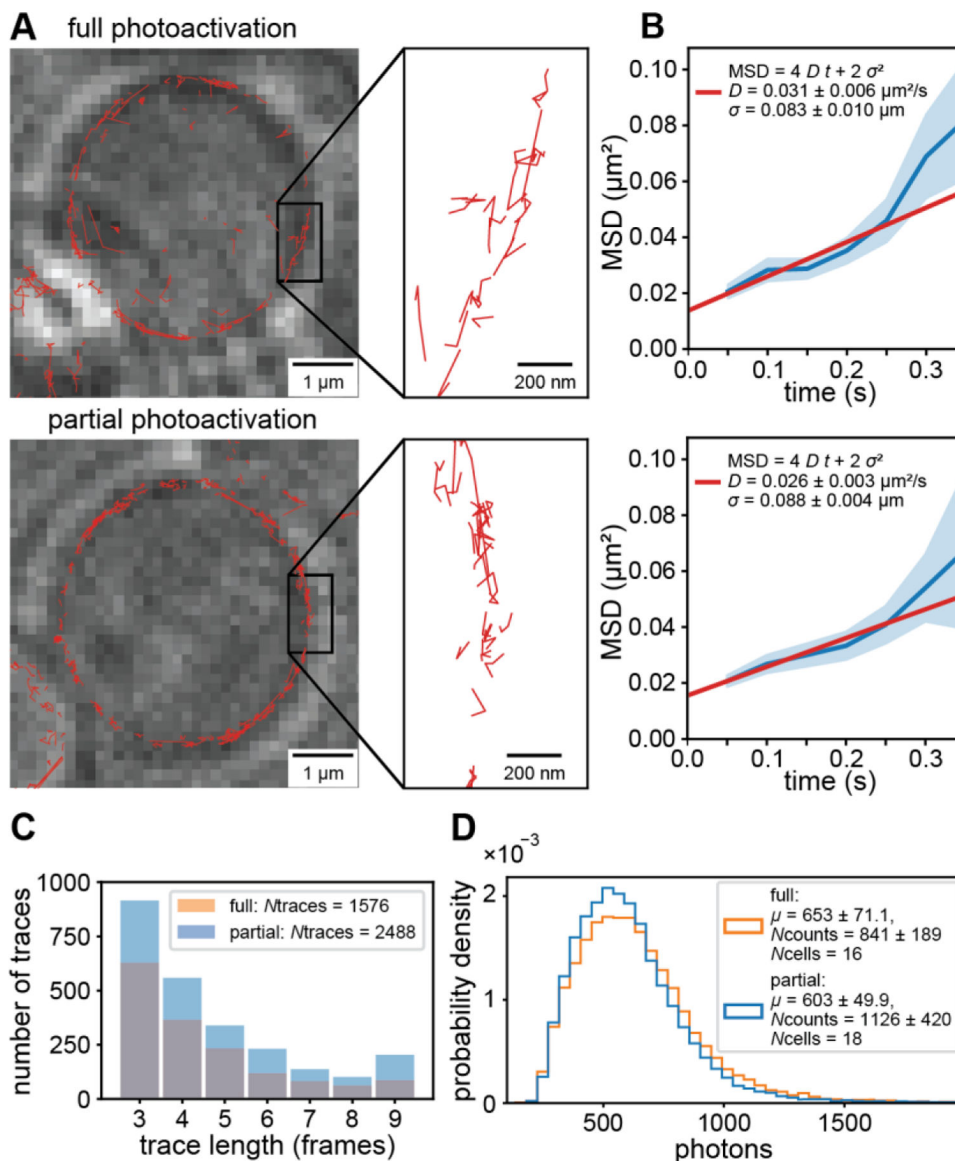
Figure 4: Comparison of single-molecule tracking with conventional and spatially informed PALM.

(A) Single-molecule traces (red) superimposed on LED images (average of 10 frames) of fully (top) and partially photoactivated cells (bottom). (B) Mean squared displacement vs. time (blue) and fit to model (red) of fully and partially illuminated cells (top and bottom, respectively). Error bands are the standard error of the mean across each lag time. (C) Distribution of trace lengths showing an increased number of detected single molecule traces of partially photoactivated cells compared to fully photoactivated cells. All single-molecule traces and localizations were analyzed up to the mean transition time to unhealthy state. (D) Probability density of photons per single-molecule localization showing that the quality of localizations is the same for fully and partially photoactivated cells.